Cyclic axial response and energy dissipation of cold-formed steel framing members

David A. Padilla-Llano *, Cristopher D. Moen, Matthew R. Eatherton

The Charles E. Via, Jr. Department of Civil & Environmental Engineering, Virginia Polytechnic Institute and State University, 200 Patton Hall, Blacksburg, VA 24061, USA

ABSTRACT

This paper summarizes results from an experimental program that investigated the cyclic axial behavior and energy dissipation of cold-formed steel C—sections structural framing members. Fully characterized cyclic axial load–deformation response of individual members is necessary to facilitate performance-based design of cold-formed steel building systems. Specimen cross-section dimensions and lengths were selected to isolate specific buckling modes (i.e., local, distortional or global buckling). The cyclic loading protocol was adapted from FEMA 461 with target displacements based on elastic buckling properties. Cyclic response showed large post-buckling deformations, pinching, strength and stiffness degradation. Damage accumulated within one half-wave after buckling. The total hysteretic energy dissipated within the damaged half-wave decreased with increasing cross-section slenderness. More energy dissipation comes at the cost of less cumulative axial deformation before tensile rupture.

1. Introduction

Current seismic analysis and design procedures for cold-formed steel (CFS) frame buildings focus on the strength of individual shear wall units [1], e.g., shear walls constructed with CFS steel members sheathed with Structural 1 plywood (4 ply), oriented strand board (OSB), gypsum board, or thin sheet steel or strap bracing. These building subsystems are designed using prescriptive procedures and tabulated values based on shear wall tests.

Research efforts to characterize the response and develop numerical models for CFS lateral load resisting systems typically focus on the response of shear walls to push-over and cyclic tests (e.g., [2–4]). Specific guidance about energy dissipation or strength degradation for these systems and their components (e.g., drag struts, boundary chord studs) is not readily available. The goal of the research summarized in this paper is to experimentally investigate and then quantify the cyclic behavior, and energy dissipation characteristics of CFS axial members. This test data will be implemented in future CFS subsystem seismic numerical models as part of a larger ongoing multi-university research effort [5].

The shift towards performance-based design in earthquake design is creating considerable interest in understanding and controlling building seismic behavior at different seismic hazard levels. To develop seismic performance factors (i.e., R, Ω_0, and C_d)

it is necessary to consider suites of ground motions, ground motion intensities and structural configurations [6] with efficient and accurate modeling tools that can simulate structural response of the structural components of CFS buildings. For example, CFS framing could be simulated with hysteretic load–deformation springs in a computationally efficient model as shown in Fig. 1, where the springs are calibrated using experimental data from cyclic tests to represent each of the members and connections. To develop this modeling capability, it is necessary to characterize cyclic behavior and energy dissipation of individual CFS systems, member components and connections.

The experimental program described herein includes twelve cyclic axial tests, 12 monotonic axial tests in compression, and two monotonic axial tests in tension, conducted on common CFS C-section studs without perforations. Cross-section dimensions and specimen length are varied to isolate local, distortional or global buckling, and a loading protocol adapted from FEMA 461 [7] is employed where the target displacements are calculated using the member elastic buckling properties. Local and global buckling slenderness are key parameters influencing energy dissipation of thin-walled steel components, and these trends are explored in a review of existing literature in the next section.

2. Cyclic response of axial members including buckling

Existing cyclic axial tests focused on hot-rolled steel structural sections used for steel-framed buildings and offshore oil platforms. The cyclic axial behavior of globally slender steel members (struts,

* Corresponding author. Tel.: +1 740 274 0492.
  E-mail addresses: dapadill@vt.edu (D.A. Padilla-Llano),
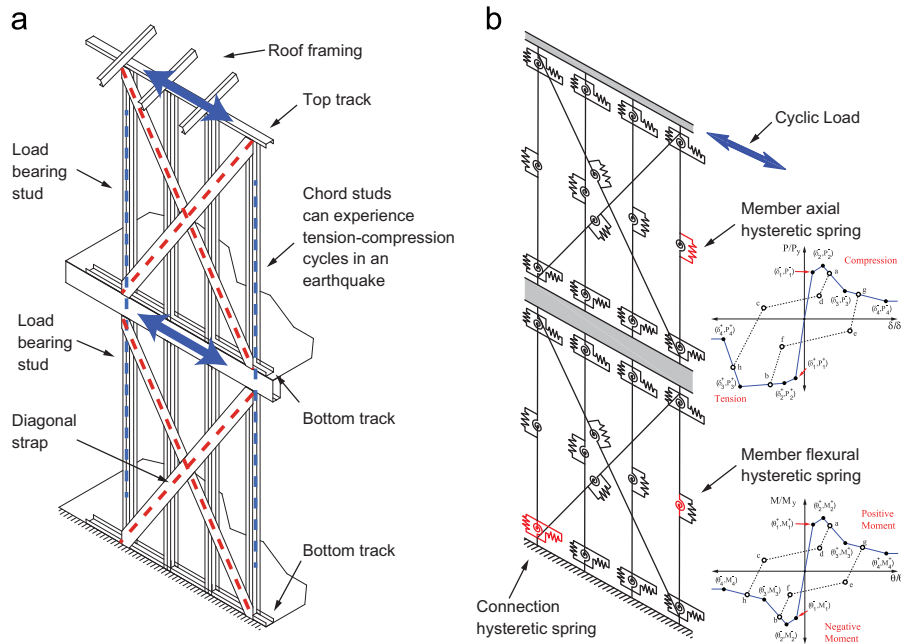cmoen@vt.edu (C.D. Moen), meather@vt.edu (M.R. Eatherton).

Fig. 1. Cold-formed strap bracing (a) and corresponding phenomenological model (b).

braces) was studied starting in the early 1970s, both analytically and with experimental programs. Hysteretic load–deformation response models for columns experiencing a plastic hinge were developed for finite element models [8–11]. Some of the models included cross-sectional slenderness as a softening parameter [12,13]. The analytical models were combined with experimental data in a few cases to develop semi-empirical equations that predict bracing member fracture life, i.e., the number of cycles to tensile fracture [14].

The viability of these numerical models was established by experiments on structural sections ranging from solid steel bars [8] to hollow thin-walled tubes [15], W-sections [16], and angles [17]. A few experiments even considered the influence of cold-bending on energy dissipation [18]. These studies have shown that, inelastic elongation of the members during tensile excursions occurred in a relatively predictable manner [8,16,17]; that tension strength remained fairly constant during inelastic cycles, but compression strength degraded with the number of cycles (implying damage accumulation in compression) [15–17]; when local buckling accompanied global deformation, the member failure mode was typically tensile fracture caused by stress concentrations at a fold [15]; that inelastic deformation of the steel was the key contributor to energy dissipation as compared to inherent material damping [17]; that the total energy dissipation appears to be independent of initial loading direction (tension then compression or compression and then tension) [17]; and, that the amount of total hysteretic energy dissipated decreases as the global slenderness increases [15,17].

Only a few experimental programs focused on energy dissipation from local buckling [19–22]. These studies showed that local buckling compression strength degraded to a constant magnitude with increasing cycles because of inherent post-buckling capacity, which is different and potentially more beneficial to seismic performance than global buckling cyclic behavior where compressive strength decreases to zero as the plastic hinge develops. The experimental program described below explores these post-buckling benefits and documents the cyclic behavior of CFS axial members with a focus on thin-walled member buckling limit states, i.e., global, distortional and local buckling.

3. Experimental program

An experimental program was conducted to study the cyclic response of CFS axial members experiencing local, distortional and global buckling. Cyclic tests were conducted to determine the effects of reversed cyclic loading (i.e., tension and compression) and cumulative axial deformation on damage and hysteretic energy dissipation of members experiencing global, distortional or local buckling. Monotonic tests were performed to establish a load–deformation envelope for comparison to the cyclic test response.

3.1. Specimen selection strategy

Specimens were selected such that their predicted monotonic capacity in compression is governed either by local, distortional or global buckling as predicted by the American Iron and Steel Institute (AISI) Direct Strength Method (AISI-S100-07, [23]). The cross-sections considered, five (5) in total with web widths of 92 mm and 152 mm and nominal thicknesses ranging from 0.88 to 2.58 mm, were chosen from standard sizes as listed in the Structural Stud Manufacturers Association (SSMA) catalog [24]. Cross-section dimensions and length (L) varied to isolate each buckling limit state. Global buckling specimens have a length $L=2286$ mm, while for distortional buckling tests $L=610$ mm and for local buckling $L=305$ mm. The test program included two specimens subjected to quasi-static cyclic displacement and two specimens subjected to monotonic displacement (in compression) per specimen type. Two monotonic tests in tension were included to define the representative tension side load–deformation envelope. Specimen nomenclature is explained in Fig. 2a.

3.2. Specimen dimensions, material properties and elastic buckling loads

Cross-section dimensions were measured at member mid-height using methods described in [25], see Table 1 and Fig. 2b. These values were input to the finite strip eigen-buckling analysis software CUFSM [26] to calculate the elastic buckling loads for

local buckling, $P_{cr\ell}$, distortional buckling, P_{crd}, and global buckling, P_{cre}, and the associated half-wavelengths ($L_{cr\ell}$, L_{crd}, and L_{cre} respectively). Boundary conditions were assumed to be warping fixed (i.e., fixed–fixed) when calculating the elastic buckling loads, i.e., an effective length of $0.5L$ is considered when calculating P_{cre}. In addition, P_{crd} was calculated including the effects of warping-fixed ends [25] and considering the increase in P_{crd} when L_{crd} is longer than the total member length [23].

The tension yield load, P_y, was determined using the measured cross-section area and the average yield stress F_y obtained from

three coupon tests per specimen. Coupon tests were conducted in accordance with ASTM E8M-04 [27] with one coupon taken from each flange and web flat. The monotonic compression capacity, P_n, was calculated using the AISI-S100-07 Direct Strength Method [23]. These values are summarized in Table 2.

3.3. Test setup and instrumentation

A uniaxial loading frame was assembled to perform the cyclic tests (see Fig. 3). End plates were welded to both ends of the
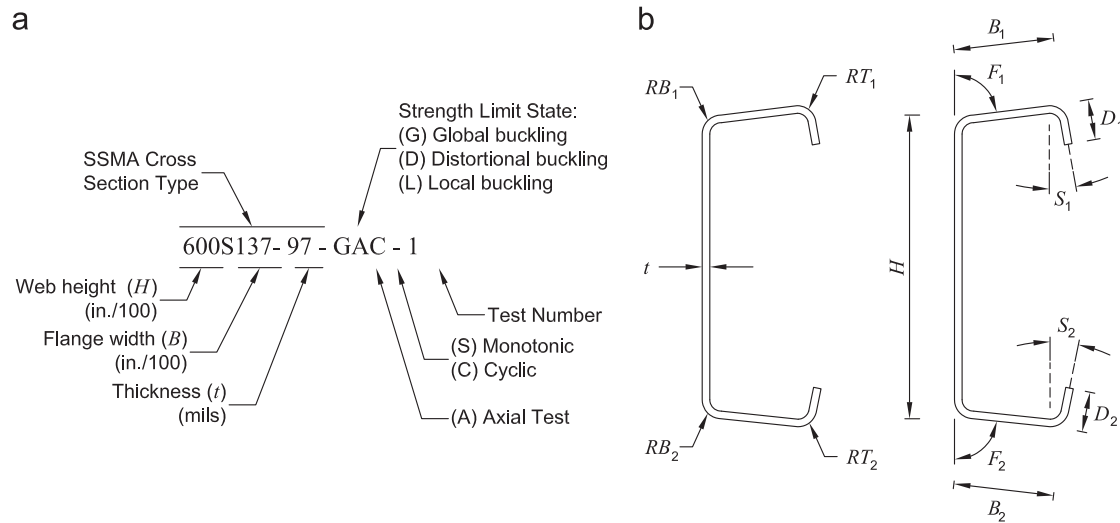

Fig. 2. Specimen naming notation (a) and cross-section dimension (b).

Table 1
Measured specimen dimensions.

Specimen	L (mm)	A_g (mm²)	D_1 (mm)	D_2 (mm)	B_1 (mm)	B_2 (mm)	H (mm)	RT_1 (mm)	RB_1 (mm)	RT_2 (mm)	RB_2 (mm)	F_1 (deg)	F_2 (deg)	S_1 (deg)	S_2 (deg)	t (mm)
600S137-97-GAM-1	2286	631	19.1	17.3	36.2	35.8	152.7	5.2	5.8	4.8	5.2	84.1	89.3	1.7	1.6	2.59
600S137-97-GAM-2	2286	632	19.1	17.5	36.1	35.7	152.2	5.0	6.0	4.8	5.2	83.8	87.9	1.6	1.9	2.60
600S137-97-GAC-1	2286	634	17.6	19.5	35.8	36.0	152.1	4.8	5.6	4.8	5.4	87.6	84.3	1.0	1.4	2.60
600S137-97-GAC-2	2286	629	17.6	18.9	35.6	35.9	152.5	4.8	5.2	5.2	6.0	87.6	85.1	3.1	2.0	2.58
362S137-68-GAM-1	2286	315	11.6	13.4	34.5	33.5	93.3	4.0	4.0	4.4	4.4	88.4	87.6	−2.5	4.8	1.82
362S137-68-GAM-2	2286	316	11.7	13.5	34.5	33.3	93.2	4.0	3.8	4.4	4.4	86.6	87.8	−3.5	3.6	1.82
362S137-68-GAC-1	2286	315	11.8	13.3	34.4	33.6	93.3	4.0	4.0	4.4	4.4	86.6	88.1	−2.0	3.4	1.82
362S137-68-GAC-2	2286	315	11.8	13.3	34.4	33.4	93.3	4.0	4.0	4.4	4.4	88.5	88.2	−2.5	4.1	1.82
600S137-68-DAM-1	610	416	10.9	11.5	34.8	33.8	152.7	4.0	3.6	4.4	4.2	90.5	88.6	−1.5	0.6	1.80
600S137-68-DAM-2	610	415	10.7	11.5	34.8	33.8	152.7	4.0	4.0	4.4	4.0	90.5	89.5	−1.4	−0.7	1.80
600S137-68-DAC-1	610	416	10.8	11.3	34.4	34.2	152.7	4.0	4.0	4.2	4.0	91.9	88.1	−1.1	5.0	1.80
600S137-68-DAC-2	610	415	10.5	11.9	34.9	33.8	152.5	4.0	4.0	4.4	4.2	89.9	89.6	−1.1	−0.1	1.80
362S137-68-DAM-1	610	318	11.9	13.4	34.8	33.5	94.0	4.0	4.0	4.4	4.4	88.8	86.9	−4.7	5.4	1.82
362S137-68-DAM-2	610	317	12.0	12.9	34.5	33.9	93.3	4.0	4.0	4.4	4.4	89.8	86.4	−2.0	4.2	1.82
362S137-68-DAC-1	610	313	11.5	13.2	34.5	33.5	93.2	4.0	4.0	4.4	4.4	87.6	88.1	−2.3	4.1	1.81
362S137-68-DAC-2	610	314	11.6	13.4	34.4	33.9	93.2	4.0	4.0	4.4	4.4	89.7	86.2	−2.1	4.0	1.81
600S162-33-LAM-1	305	215	12.9	13.6	42.1	41.7	149.9	3.6	4.2	3.4	4.4	84.4	90.7	5.2	1.6	0.86
600S162-33-LAM-2	305	215	13.0	13.5	42.0	41.5	150.3	3.6	4.0	3.6	4.4	88.1	91.9	2.0	−0.2	0.86
600S162-33-LAC-1	305	215	12.7	13.6	41.9	41.7	150.6	3.6	4.0	3.6	4.4	84.6	91.1	6.0	1.5	0.86
600S162-33-LAC-2	305	215	12.7	13.6	41.9	41.5	150.3	3.6	4.0	3.2	4.4	86.6	89.1	3.1	3.6	0.86
362S162-54-LAM-1	305	272	12.0	11.6	41.6	42.3	93.1	3.6	4.4	4.2	4.4	90.2	89.8	0.9	2.4	1.44
362S162-54-LAM-2	305	273	11.7	12.2	42.3	41.6	92.7	4.2	4.4	3.6	4.4	89.2	89.2	3.2	2.2	1.44
362S162-54-LAC-1	305	272	11.7	11.8	42.0	41.6	92.7	4.0	4.4	3.6	4.4	88.9	89.5	1.0	2.0	1.44
362S162-54-LAC-2	305	273	11.8	12.0	42.3	41.7	92.9	4.2	4.4	3.8	4.4	89.0	89.2	5.1	2.3	1.44
362S162-54-LAMT-1	305	272	11.8	12.3	41.1	42.2	92.8	3.6	4.2	4.0	4.2	92.4	88.8	−3.6	3.6	1.46
362S162-54-LAMT-2	305	274	11.7	12.2	41.3	42.3	93.9	3.6	4.4	4.2	4.3	90.1	88.1	1.4	3.9	1.46

See the dimension definitions in Fig. 2.

specimens to transfer axial forces while providing rotation fixed, twist fixed, and longitudinal warping fixed end boundary conditions. Specimen axial deformations were measured using two LVDTs connected between the top and bottom end plates as shown on the right inset of Fig. 3. Specimens were subjected to a cyclic displacement history at a constant displacement rate of 0.008 (mm/mm)/(min). Based on previous monotonic tension coupon tests, it is expected that this displacement rate will produce yield stresses approximately about 2% larger than the static yield stress while minimizing strain-rate related effects [28]. The displacement rate for the monotonic tests was set to 0.0001 (mm/mm)/(min), which corresponds to the maximum rate of 21 MPa/min recommended in the AISI-S910-08 test method for column distortional buckling [29].

3.4. Loading protocol

The loading protocol (see Fig. 4) was adapted from FEMA 461 quasi-static cyclic deformation-controlled testing protocol. The FEMA 461 protocol is used to obtain fragility data and hysteretic load–deformation response characteristics of building components for which damage is best predicted by imposed deformations [7]. CFS axial members may experience asymmetrical loading because of end connections (e.g., screwed or welded connection) and the location within a building system (e.g., end stud compared to an inside stud in a shear wall). Using a symmetric protocol with equal deformation demands in compression and tension captures the damage and energy dissipation from cross-sectional deformation of the thin-walled channel sections under compression and damage and tearing that can occur by the reversal of these deformations under tension loading. Hysteretic numerical models built based on the responses obtained from this protocol are expected to be capable of capturing the behavior under different loading patterns such as on-sided loading.

The loading protocol consists of amplitude increasing steps with two cycles per step. Each step amplitude is related to the previous by the equation $\delta_i = 1.4\delta_{i-1}$ (see Fig. 4). The anchor point is the elastic axial displacement, $\delta_e = P_e L / AE$, that defines the amplitude of the fourth step (i.e., 7th and 8th cycles). The compressive load, P_e, at which buckling deformations influence the load–deformation response is calculated using slenderness limits defined in the AISI-S100-07 DSM [23]. The DSM approach predicts that local buckling deformation initiates at $\lambda_\ell = 0.776$ and the distortional buckling deformation initiates at $\lambda_d = 0.561$. Using $\lambda = (P_e/P_{cr})^{0.5}$, then $P_e = 0.60 \ P_{cr\ell}$ and $P_e = 0.31 P_{crd}$. The load where global buckling deformation influences load–deformation response is assumed to be $P_e = 0.50 P_{cre}$. Values of δ_e are listed in Table 2 for all specimens.

3.5. Specimen imperfections

Initial geometric imperfections in CFS members reduce axial strength and initial stiffness in compression. The measured strength, as well as the predicted strength from a FEM analysis that includes imperfections, decreases the most if the shape of imperfections resemble the governing buckling modes [25,30,31]. Member imperfections are defined as the specimen geometry deviations from the straight "perfect" member before attaching it to the loading frame (see Fig. 5). Imperfections were measured using methods described in [32].

The average maximum measured imperfections were generally smaller than the tolerance limits given in ASTM C955-09 [33] as shown in Table 3. However, for some specimens the global imperfections where larger than the ASTM limit and affected their strength. For instance, the strength of specimen 600S137-97-GAM-2 was 17%

Table 2
Elastic buckling properties and predicted compressive capacity.

Specimen	F_y (MPa)	F_u (MPa)	P_y (kN)	P_n (kN)	P_{cre} (kN)	λ_e	P_{crd} (kN)	λ_d	L_{crd} (mm)	$P_{cr\ell}$ (kN)	λ_ℓ	$L_{cr\ell}$ (mm)	δ_e ($\times 10^{-3}$mm)
600S137-97-GAM-1	388	529	245	121	147	1.29	228	1.04	314	198	0.78	119	654
600S137-97-GAM-2	394	529	249	122	147	1.30	232	1.04	314	201	0.78	118	653
600S137-97-GAC-1	382	523	242	121	147	1.28	233	1.02	318	202	0.78	118	650
600S137-97-GAC-2	388	528	244	120	145	1.30	225	1.04	315	196	0.78	119	647
362S137-68-GAM-1	392	531	123	60	71	1.32	165	0.86	253	130	0.68	71	636
362S137-68-GAM-2	387	529	122	59	70	1.32	167	0.86	252	131	0.67	71	624
362S137-68-GAC-1	389	535	123	59	70	1.32	166	0.86	254	130	0.67	71	626
362S137-68-GAC-2	386	529	121	60	71	1.30	165	0.86	254	130	0.68	71	638
600S137-68-DAM-1	427	558	177	91	1249	0.38	76	1.53	260	62	1.64	123	173
600S137-68-DAM-2	427	558	177	90	1243	0.38	75	1.53	258	62	1.64	124	172
600S137-68-DAC-1	427	558	177	91	1270	0.37	76	1.53	259	62	1.64	124	172
600S137-68-DAC-2	427	558	177	91	1256	0.38	76	1.53	259	62	1.64	123	173
362S137-68-DAM-1	389	529	124	103	968	0.36	180	0.83	256	130	0.95	72	533
362S137-68-DAM-2	389	529	123	103	961	0.36	180	0.83	255	132	0.94	71	537
362S137-68-DAC-1	389	528	122	101	933	0.36	175	0.83	252	128	0.95	71	529
362S137-68-DAC-2	389	528	122	102	947	0.36	177	0.83	254	128	0.95	71	531
600S162-33-LAM-1	333	398	72	27	4138	0.13	62	1.08	515	8	3.04	111	32
600S162-33-LAM-2	333	398	72	32	4307	0.13	53	1.16	462	11	2.49	108	48
600S162-33-LAC-1	333	398	72	27	4125	0.13	60	1.09	512	8	3.05	112	32
600S162-33-LAC-2	333	398	72	27	4147	0.13	60	1.09	511	8	3.05	111	32
362S162-54-LAM-1	416	476	113	81	3704	0.17	157	0.85	330	70	1.26	72	232
362S162-54-LAM-2	416	476	113	81	3674	0.18	160	0.84	333	71	1.26	71	234
362S162-54-LAC-1	416	476	113	81	3626	0.18	157	0.85	328	70	1.26	71	233
362S162-54-LAC-2	416	476	113	81	3683	0.18	158	0.85	332	70	1.26	72	232
362S162-54-LAMT-1	416	476	113	81	3717	0.17	161	0.84	334	70	1.26	71	233
362S162-54-LAMT-2	416	476	114	81	3720	0.17	159	0.85	332	69	1.27	72	228

$\lambda_e = (P_y/P_{cre})^{0.5}$; $\lambda_d = (P_y/P_{crd})^{0.5}$; $(\lambda_\ell = (P_{ne}/P_{cr\ell})^{0.5}$.
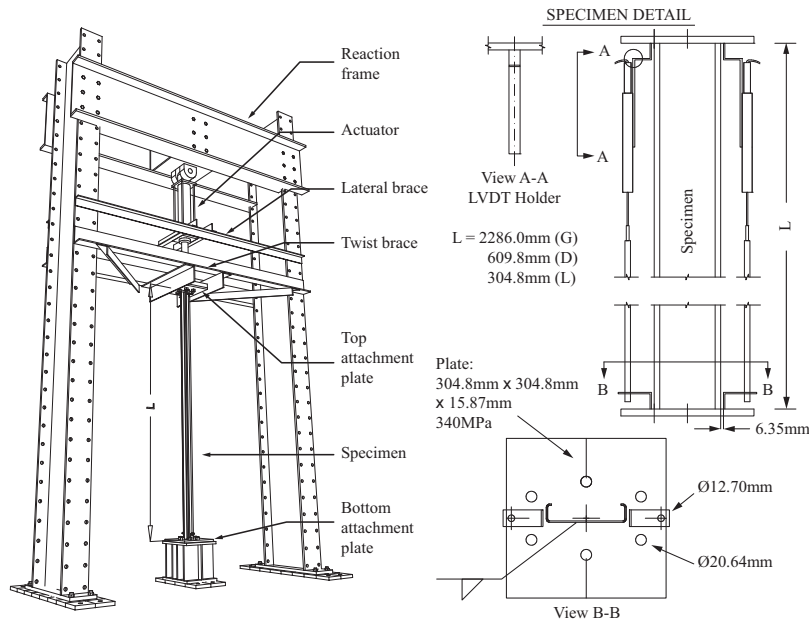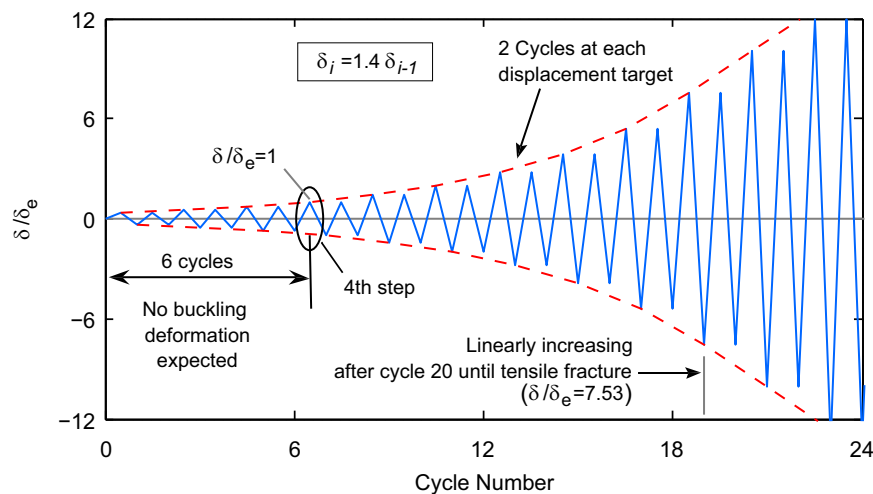
Fig. 3. Test setup and specimen detail.

Fig. 4. Cyclic compression–tension cold-formed steel loading protocol.

lower than the predicted strength (see Table 4 and Fig. 7b) due to large initial global imperfections ($\delta_B = L/452$, see Table 3) in the weak axis direction. Global imperfection magnitudes in CFS members are known to increase with sheet thickness because of plastic strains and associated residual curvature caused by coiling the sheet for transportation and manufacturing [34,31]. Initial global imperfections also affected the buckling mode. For example, specimen 362S137-68-GAM-1 experienced flexural-torsional buckling due to an initial twist $\phi = 3.93°$, the largest observed. Out-of-straightness in the strong axis direction, δ_C, for local buckling specimens was on average larger than the ASTM limits; however, its effect on compressive strength and buckling mode is negligible.

Local imperfections were all lower than ASTM limits and smaller than $\delta_w/t = 0.66$ and $\delta_f/t = 3.44$ associated with occurrence probabilities $P(\delta < \delta_w) = 0.75$ and $P(\delta < \delta_f) = 0.95$ respectively in [35]. The influence of local imperfections on the strength was negligible for all specimens, however it affected the initial stiffness of the 362DAM and the LAM specimens. Imperfection influence was negligible for members under cyclic loading because during the first elastic tension excursions the imperfections straighten

out. The result is equal initial stiffness in compression and tension (see Figs. 6a, 8a, and 10a). A detailed discussion about the measured imperfections from this testing program and their characterization can be found in [32].

4. Experimental results

4.1. Monotonic and cyclic response

Cyclic and monotonic load–deformation responses were obtained for specimens experiencing local, distortional, and global buckling. From the monotonic tests, the average ratio of test peak load (in compression) to predicted load P_{min}/P_n was 1.00 with a coefficient of variation of 0.09 (see Table 5). This result confirms that the actual boundary conditions accurately represent the assumed constraints of rotational fixity and warping fixity at the specimen ends. The cyclic response is linear during the first six cycles with equal stiffness in tension and compression for all specimens (see Figs. 6a, 8a, and 10a). As expected, the
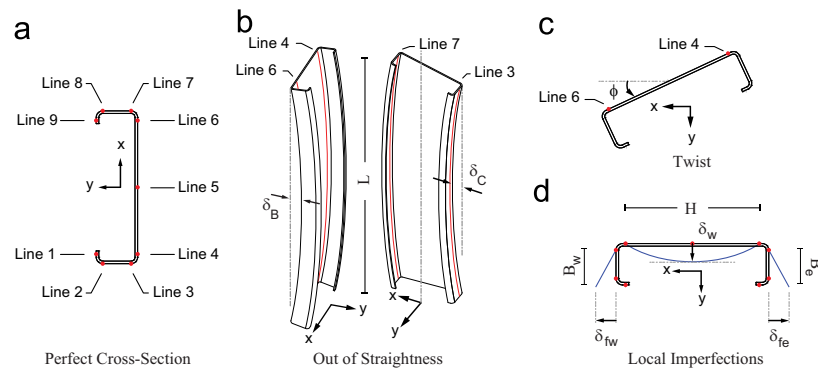
Fig. 5. Global and local imperfection definition.

Table 3
Maximum measured imperfections.

	Member imperfections											
	δ_B/L ($\times 10^{-3}$)		δ_C/L [a] ($\times 10^{-3}$)		ϕ (deg)	δ_W/H ($\times 10^{-3}$)		δ_{FE}/B_e ($\times 10^{-3}$)		δ_{FW}/B_w ($\times 10^{-3}$)	
Global											
Mean	1.04	(L/961)	–		2.64	8.16	(H/123)	48.16	(B/21)	46.27	(B/22)
Max	2.21	(L/452)	–		3.93	44.45	(H/22)	76.40	(B/13)	86.99	(B/11)
Min	0.22	(L/4556)	–		1.66	1.67	(H/598)	19.14	(B/52)	26.91	(B/37)
St. Dev	0.70		–		0.78	14.69		18.65		21.49	
COV	0.68		–		0.29	1.80		0.39		0.46	
Distortional											
Mean	0.60	(L/1678)	0.56	(L/1771)	1.39	3.25	(H/308)	41.50	(B/24)	28.25	(B/35)
Max	0.97	(L/1028)	0.95	(L/1052)	3.48	6.14	(H/163)	54.10	(B/18)	51.22	(B/20)
Min	0.23	(L/4389)	0.30	(L/3288)	0.10	0.81	(H/1231)	14.58	(B/69)	9.68	(B/103)
St. Dev	0.23		0.27		1.13	1.95		12.77		13.40	
COV	0.38		0.49		0.81	0.60		0.31		0.47	
Local											
Mean	0.46	(L/2187)	1.63	(L/612)	0.77	3.74	(H/267)	43.87	(B/23)	37.57	(B/27)
Max	0.78	(L/1277)	3.22	(L/311)	2.16	10.58	(H/95)	79.92	(B/13)	51.46	(B/19)
Min	0.20	(L/5080)	0.80	(L/1252)	0.02	1.66	(H/604)	12.24	(B/82)	22.45	(B/45)
St. Dev	0.20		1.09		0.71	2.87		23.98		12.50	
COV	0.44		0.67		0.92	0.77		0.55		0.33	
ASTM C955 Tol.	L/960		L/960		L/H/384	2×1.59 mm^2 (max)		2×1.59 mm^2 (max)		2×1.59 mm^2 (max)	

cyclic response is asymmetric due to the presence of buckling deformations in compression. Strength and stiffness in compression degraded under cycling loading due to inelastic deformations. Additional details for each of the limit states are discussed in the following sections and test videos are available at the Virginia Polytechnic Institute and State University digital repository [36].

4.1.1. Global buckling limit state

Cyclic response of global buckling (GAC) specimens was characterized by weak-axis flexural buckling, which in later cycles led to folding of the stiffening lips near the mid-height as shown in Fig. 6d. Damage from strain reversal accumulated at the mid-height in the C-section flange stiffening lips during subsequent excursions in tension and compression. Compressive strength degraded rapidly in the cycles after the peak compressive load was reached due to the damaged accumulated at the folded lips. This deterioration is quantified as the difference between the monotonic curves and the compression side of the cyclic responses in Fig. 7.

Unloading stiffness also deteriorated during cyclic loading and the member unloaded nonlinearly from the compression side as shown in Fig. 6b. Web inelastic buckling occurred near the supports after damage accumulated at the mid-height folded lips.

Excursions in tension after peak compressive load is reached were characterized by very low stiffness until the member straightens out as shown in Fig. 6b. Ductile yielding at a consistent tension yield capacity was observed at the mid-height cross-section as shown in bottom-left quadrant of Fig. 6c. The final failure mode was gradual tearing of the section starting at the folded lips and propagating through the cross section, or in some cases fracture near the welded connection.

The monotonic response of the global buckling (GAM) specimens was generally characterized by weak axis flexural buckling, with folding of the stiffening lips at mid-height. Specimen 362S137-68-GAM-1 however, exhibited flexural-torsional buckling due to torsional initial imperfections in the member. This resulted in a higher peak compression load and higher monotonic envelope as shown in Fig. 7a and Table 4.

4.1.2. Local buckling limit state

Cyclic response of the local buckling (LAC) specimens was characterized by web buckling with at least two half-waves occurring before reaching the peak compressive load. After the peak load in compression, one half-wave locked around mid-height and damage accumulated at that location (see Fig. 8d). Compressive strength and unloading stiffness then degraded quickly on the compression side as shown in Fig. 8b and c; however unlike global buckling members,

Table 4
Test maximum loads.

Specimen	P_{max} (kN)	δ_{Pmax} ($\times 10^{-3}$ mm)	P_{min} (kN)	δ_{Pmin} ($\times 10^{-3}$ mm)	δ_y ($\times 10^{-3}$ mm)	P_{max}/P_y	P_{min}/P_n	δ_{Pmax}/L ($\times 10^{-3}$)	δ_{Pmin}/L	δ_{Pmax}/δ_y	δ_{Pmin}/δ_y
600S137-97-GAM-1	–	–	−117	−2413	4358	–	0.97	–	−1.06	–	−0.55
600S137-97-GAM-2	–	–	−101	−2921	4424	–	0.83	–	−1.28	–	−0.66
600S137-97-GAC-1	236	8890	−129	−2362	4289	0.98	1.06	3.89	−1.03	2.07	−0.55
600S137-97-GAC-2	237	16,180	−127	−2388	4361	0.97	1.06	7.08	−1.04	3.71	−0.55
362S137-68-GAM-1	–	–	−56	−2718	4400	–	0.94	–	−1.19	–	−0.62
362S137-68-GAM-2	–	–	−53	−2362	4355	–	0.90	–	−1.03	–	−0.54
362S137-68-GAC-1	122	8331	−50	−2464	4376	1.00	0.84	3.64	−1.08	1.90	−0.56
362S137-68-GAC-2	123	9068	−49	−2261	4339	1.01	0.83	3.97	−0.99	2.09	−0.52
600S137-68-DAM-1	–	–	−97	−1829	1277	–	1.07	–	−3.00	–	−1.43
600S137-68-DAM-2	–	–	−97	−1626	1279	–	1.08	–	−2.67	–	−1.27
600S137-68-DAC-1	175	3226	−96	−1295	1279	0.99	1.06	5.29	−2.13	2.52	−1.01
600S137-68-DAC-2	174	2769	−100	−1118	1278	0.98	1.10	4.54	−1.83	2.17	−0.87
362S137-68-DAM-1	–	–	−100	−1778	1166	–	0.96	–	−2.92	–	−1.52
362S137-68-DAM-2	–	–	−98	−1499	1166	–	0.95	–	−2.46	–	−1.28
362S137-68-DAC-1	127	5512	−99	−1168	1167	1.05	0.98	9.04	−1.92	4.72	−1.00
362S137-68-DAC-2	128	5766	−96	−991	1167	1.05	0.94	9.46	−1.63	4.94	−0.85
600S162-33-LAM-1	–	–	−31	−406	499	–	1.12	–	−1.33	–	−0.82
600S162-33-LAM-2	–	–	−33	−559	499	–	1.04	–	−1.83	–	−1.12
600S162-33-LAC-1	66	838	−29	−457	499	0.92	1.06	2.75	−1.50	1.68	−0.92
600S162-33-LAC-2	67	991	−32	−457	499	0.94	1.19	3.25	−1.50	1.99	−0.92
362S162-54-LAM-1	–	–	−88	−813	623	–	1.08	–	−2.67	–	−1.31
362S162-54-LAM-2	–	–	−86	−889	623	–	1.05	–	−2.92	–	−1.43
362S162-54-LAC-1	109	1295	−88	−508	623	0.97	1.08	4.25	−1.67	2.08	−0.82
362S162-54-LAC-2	110	1270	−90	−635	623	0.97	1.11	4.17	−2.08	2.04	−1.02
362S162-54-LAMT-1	110	1719	–	–	623	0.97	–	5.64	–	2.76	–
362S162-54-LAMT-2	115	9896	–	–	623	1.01	–	32.47	–	15.89	–

P_{max}, δ_{Pmax}=test max tension and corresponding displacement; P_{min}, δ_{Pmin}=test max compression and corresponding displacement. $\delta_y=P_yL/EA_g$ the elastic yielding displacement.

unloading from compression was linear for all excursions (see Fig. 9). The difference between the monotonic curves and the compression side of the cyclic responses in Fig. 9 demonstrates this deterioration. Strength in tension deteriorated faster in the 600LAC specimens than for the 362LAC specimens. The 362LAC specimens experienced yielding close to the rounded corners and a yield line across the web. Tearing started thereafter at the center of the web and propagated to the corners and then to the rest of the cross-section. The 600LAC specimens exhibited similar behavior, but as shown in Fig. 8d, two yield lines formed around mid-height where tearing occurred. The 600LAC specimens underwent approximately 100 cycles after which the web was still carrying some tensile load.

The monotonic response of the local buckling (LAM) specimens demonstrated similar deformations as their cyclic counterpart; however, in the 362LAM specimens these deformations occurred closer to the top end plate. Initial stiffness for the 362LAM specimens was lower than for their cyclic counterparts from initial imperfections (see Fig. 9a). Both cyclic and monotonic tests exceeded the predicted compressive capacity P_n, but the maximum tensile strength fell below the yield load P_y for the 600LAC specimens (see Table 4). It is hypothesized that for thinner members (e.g., 600S162-33-LAC) the flanges and corners carried more of the tensile load than the web, and therefore, the cross-section was not fully effective in tension. This as a consequence of the large web buckling deformations during compression excursions that did not fully straightened out when loading in tension leading to non-uniform tension yielding around the cross-section.

4.1.3. Distortional buckling limit state

Cyclic response of the distortional buckling 600DAC specimens was characterized by the formation of at least one half-wavelength centered at mid-height as seen in Fig. 10d. Damage accumulated from inelastic strains at the rounded corners as the member stretched and

compressed. Strength in compression and unloading stiffness degraded from inelastic strains accumulating in the damaged half-wave as shown by the difference between the monotonic curves and the cyclic envelopes in Fig. 11. The strength in tension remained constant until tearing started at the rounded corners and propagated around the cross section. The deformations experienced by the 362DAC specimens were a combination of distortional and local buckling of the web near one of the end plates. However, web buckling deformations were more visually noticeable than opening of the flanges. The behavior of the 362DAC members was found to be similar to the behavior of the local buckling 362LAC specimens.

The monotonic response of the DAM specimens demonstrated similar deformations as their cyclic counterpart. Their initial stiffness however, is lower than for the DAC specimens, as seen in Fig. 11, due to initial imperfections.

4.1.4. Monotonic tension response

The monotonic tension response of the 362LAMT specimens was linear up to 80% of the peak tension load (P_{max}) when yielding starts in the web, then a short nonlinear segment caused by the propagation of yielding around the cross-section. A linear segment with decreased stiffness and large axial deformations followed to the peak tension load (see Fig. 12). Strength reduced rapidly when tearing started. The normalized axial deformations δ/δ_y far exceeded ($\sim$300% at rupture) the maximum normalized deformations reached during the tension excursions by any of the specimens that underwent cyclic loading (see Table 4). Thus, ductility in axial tension is highly reduced as a consequence of the reversal of inelastic strains at the damaged half-wave during cyclic loading (see Figs. 6–8). The monotonic responses when normalized to P_y and δ_y shown in Fig. 12 are considered here as representative of the behavior in tension of all the tested CFS members.
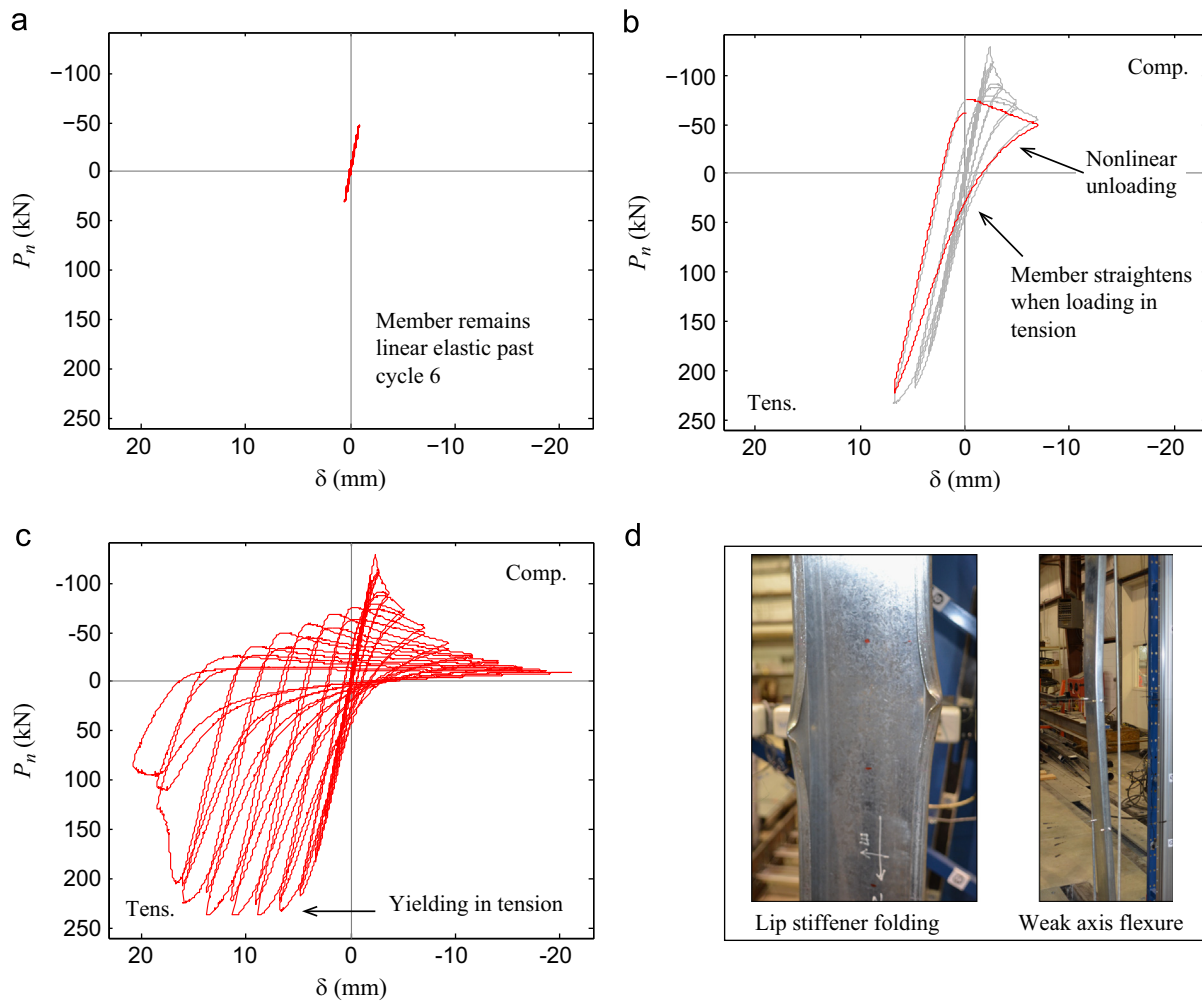
Fig. 6. Cyclic load–deformation response specimen 600S137-97-GAC-1: (a) 6 cycles; (b) 20 cycles; (c) complete response and (d) failure mode.
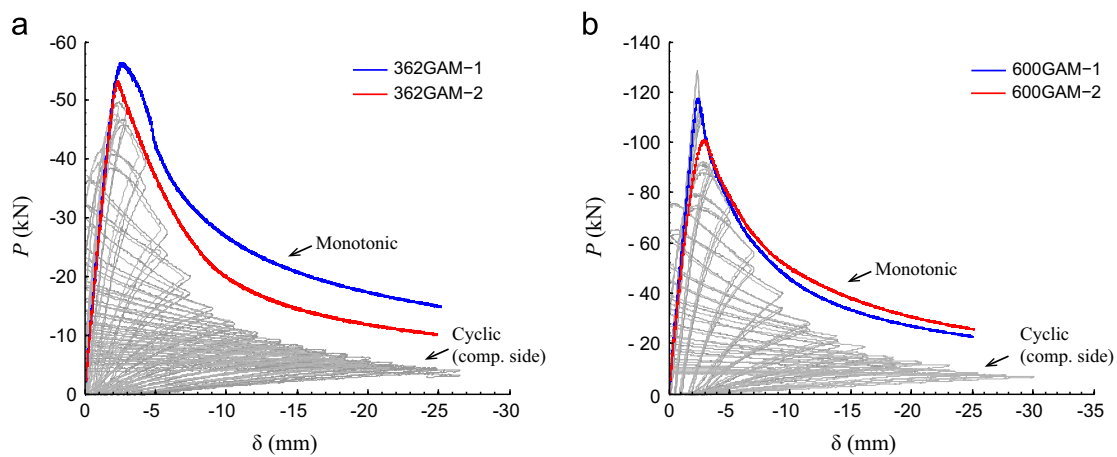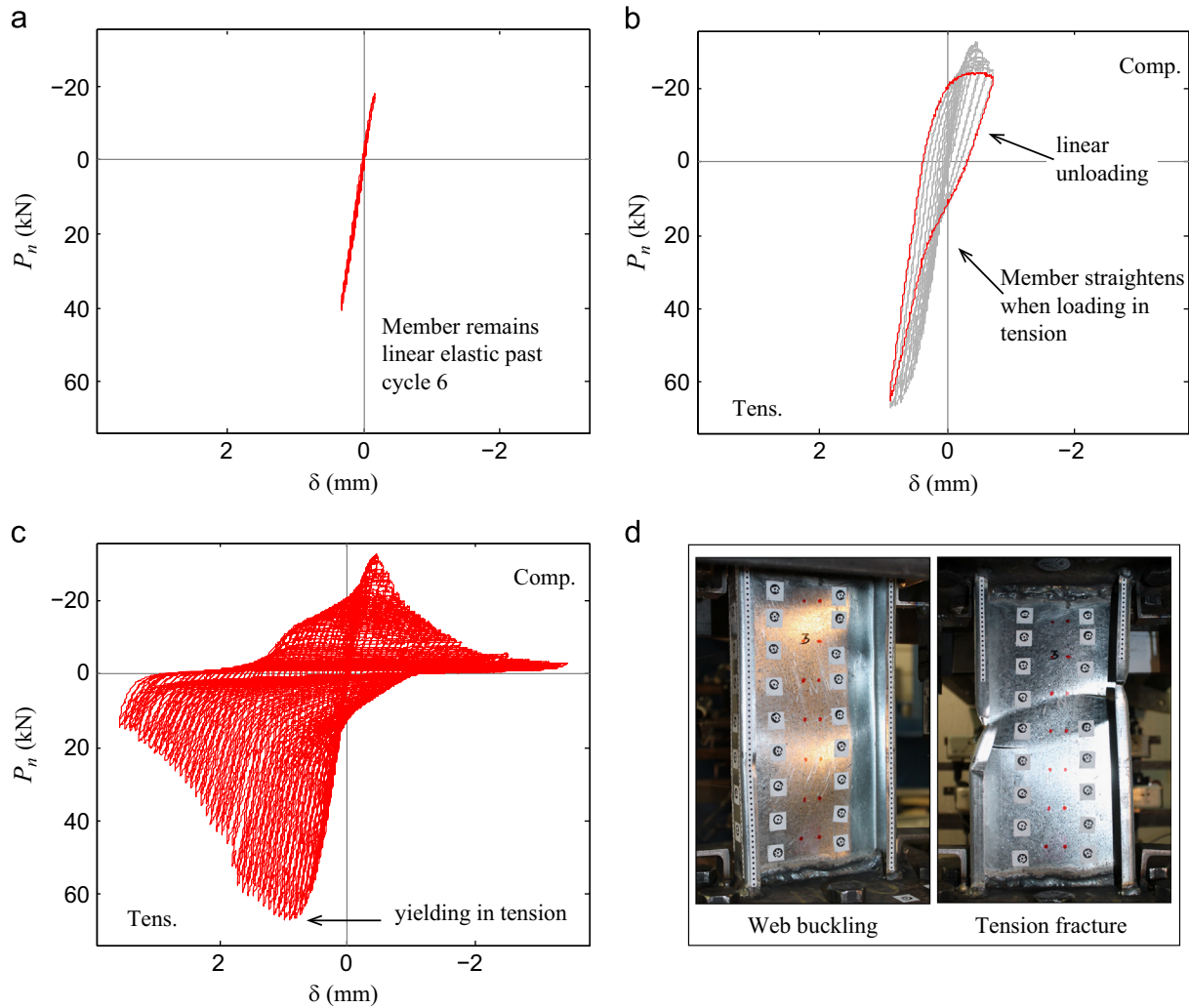

Fig. 7. Global buckling monotonic response envelope: (a) 362 series and (b) 600 series (tension side of the cyclic responses has been omitted).

4.2. Hysteretic load–deformation response and energy dissipation comparisons

Strength degradation, stiffness degradation, and pinching of the load–deformation response varies for the different specimens; however, trends can be identified by focusing in on cross-sectional slenderness. Fig. 13 compares the normalized envelopes of the cyclic response of all the specimens in this study. It can be seen that all the specimens have the same normalized pre-buckling stiffness k/k_e

($k_e{=}AE/L$). Strength in compression, compared to the peak compression load, decreased in all specimens at similar rates as the axial deformation δ/δ_y increased ($\delta_y{=}P_y/k_e$). The maximum normalized axial deformations δ/δ_y for compressions and tension excursions was similar for all the specimens. This result will be useful in the future for defining load–deformation hysteretic numerical models for CFS axial members based on a common displacement criteria.

Even though the cyclic envelopes in Fig. 13 and in general the cyclic behavior is similar for all the specimens, there

Fig. 8. Cyclic load–deformation response specimen 600S162-33-LAC-2: (a) 6 cycles; (b) 20 cycles; (c) complete response and (d) failure mode.
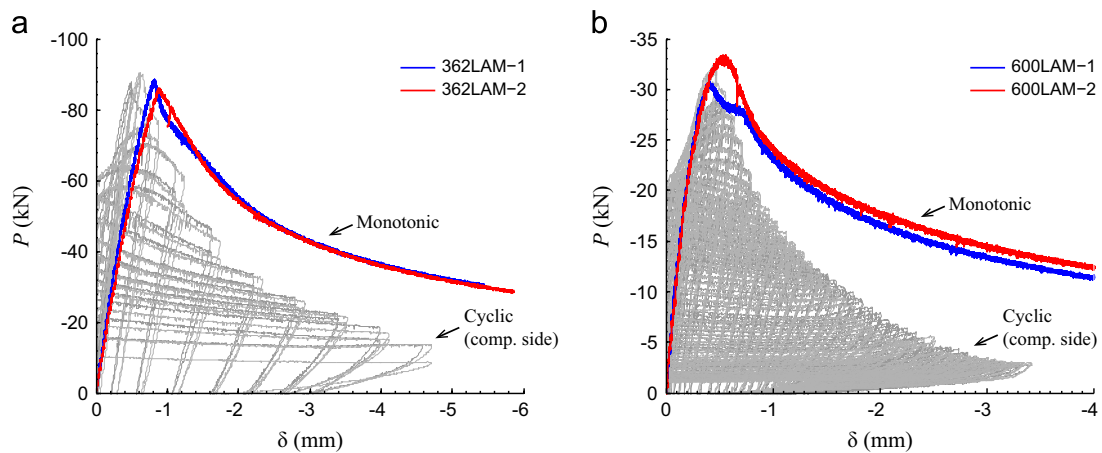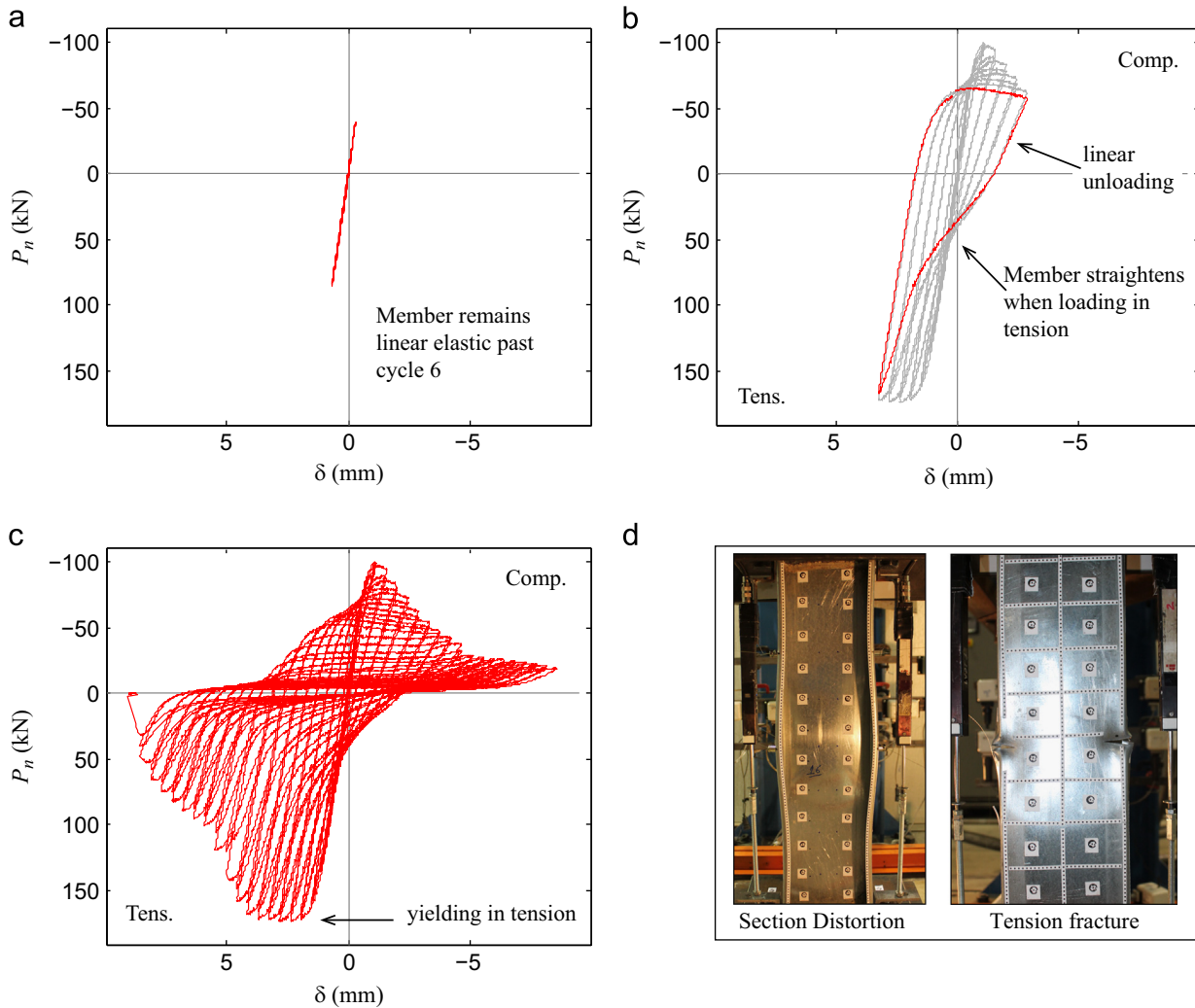

Fig. 9. Local buckling monotonic response envelope: (a) 362 series and (b) 600 series (tension side of the cyclic responses has been omitted).

are differences in the cyclic response. Specimens with smaller cross-sectional slenderness exhibited less pinching of the load–deformation response and differences in the amount of hysteretic energy dissipated. Fig. 14 compares the normalized hysteretic energy per cycle as a function of cumulative axial displacement $\Sigma\delta/L$. The hysteretic energy dissipated each cycle E_{ci} was

normalized to the area of the rectangle E_{cr} bounded by the maximum and minimum axial deformation experienced in that cycle and the predicted strengths in compression and tension (see inset in Fig. 14). The energy curves for the 362LAC and 362DAC specimens show the largest per cycle energy dissipation values (higher than 0.35), with less cumulative axial deformation before

Fig. 10. Cyclic load–deformation response specimen 600S137-68-DAC-2: (a) 6 cycles; (b) 20 cycles; (c) complete response and (d) failure mode.

Table 5
Test-to-predicted statistics.

Specimen Group	P_{max}/P_y		P_{min}/P_n		δ_{Pmax}/L		δ_{Pmin}/L		δ_{Pmax}/δ_y		δ_{Pmin}/δ_y	
	μ	Cov	μ	Cov	μ	Cov	μ	Cov	μ	Cov	μ	Cov
Global	0.99	0.02	0.93	0.10	4.64	0.35	1.09	0.09	2.44	0.35	0.57	0.08
Distortional	1.02	0.03	1.02	0.07	7.08	0.36	2.32	0.22	3.59	0.40	1.16	0.22
Local	0.95	0.02	1.09	0.04	3.60	0.20	1.94	0.30	1.95	0.09	1.04	0.22
Monotonic	–	–	1.00	0.09	–	–	2.03	0.40	–	–	1.05	0.36
Cyclic	0.99	0.04	1.03	0.11	5.11	0.43	1.53	0.27	2.66	0.43	0.80	0.25
All Spec.	0.99	0.04	1.01	0.10	5.11	0.43	1.78	0.38	2.66	0.43	0.92	0.35

μ=mean value; cov=coefficient of variation; tension tests are not included.

tensile rupture, see Table 6. The global buckling specimens (GAC) exhibit the least energy dissipation because of severe pinching in the load–deformation response. Post-peak deformations for the GAC specimens involved out-of-plane member deformations and development of plastic hinges all through the cross-section at mid-height that reduced axial stiffness. For instance, for the GAC specimens the unloading stiffness in average reduced to $0.13k_e$ for just a 10% of the total energy dissipated. Full plastic hinges did not form in the local (LAC) and distortional (DAC) buckling specimens, and therefore the axial stiffness degraded less. In this case, the unloading stiffness reduced in average to $0.47k_e$ for the same 10% of the total energy dissipated (compared to 87% in the GAC

specimens). The higher post-peak unloading stiffness from compression to tension in the LAC and DAC specimens led to less pinching of the load–deformation response and more energy dissipated per cycle.

Energy dissipation (per cycle and total) decreased with increasing cross-sectional slenderness within the damaged half-wave as shown in Fig. 15 and Table 6, results consistent with previous studies, see [19–22]. Specimens with lower cross-sectional slenderness, e.g., 362LAC ($\lambda_\ell = 1.26$) and 362DAC ($\lambda_d = 0.83$), dissipate more energy within the damaged half-wave. Less slender members (λ_ℓ, $\lambda_d \leq 1.3$—locally stocky) experience more inelastic buckling strains that translate to more damage accumulated per cycle
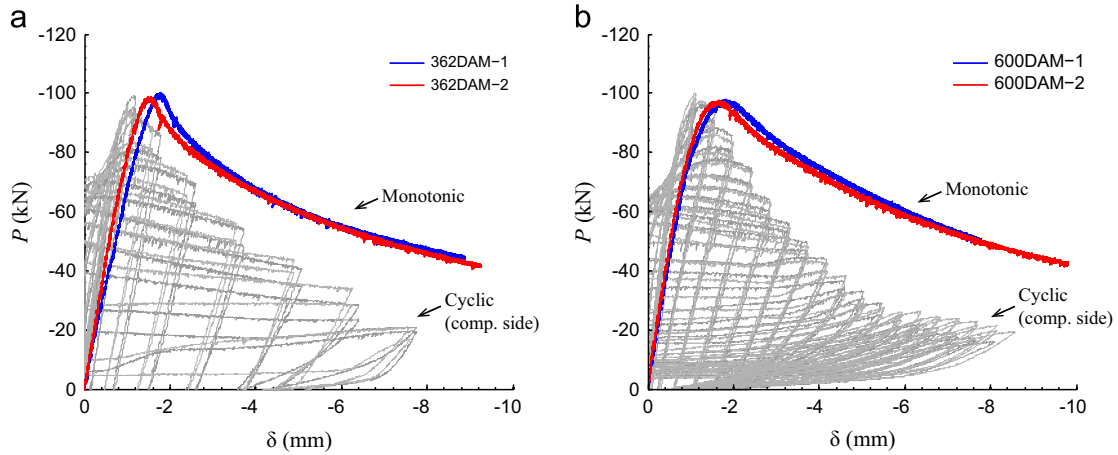
Fig. 11. Distortional buckling monotonic response envelope: (a) 362 series and (b) 600 series (tension side of the cyclic responses has been omitted).
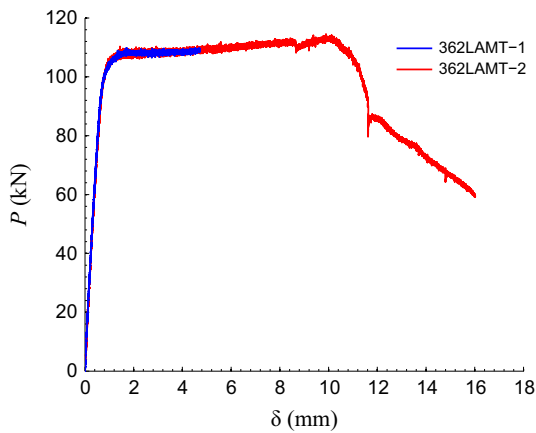

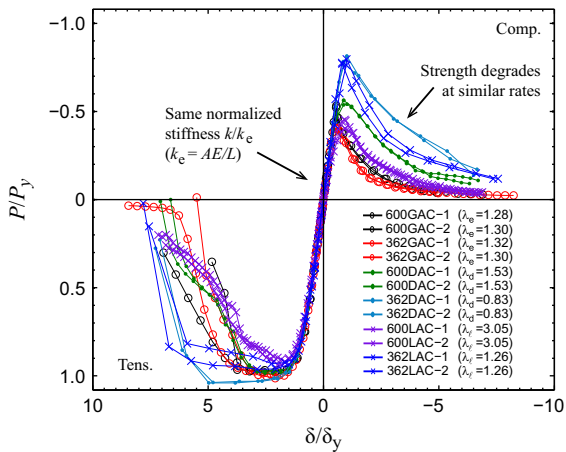**Fig. 12.** Monotonic tension response of 362LAMT specimens.

Fig. 13. Cyclic response envelopes.

Fig. 14. Hysteretic energy per cycle (normalized) vs. cumulative axial deformation.

deformations before tensile rupture when compared to the other buckling limit states.

5. Conclusion

The axial cyclic response of cold-formed steel C-section framing members experiencing local, distortional and global buckling was investigated. Twelve cyclic tests, 12 monotonic tests in compression, and two monotonic tests in tension were performed to evaluate the hysteretic load–deformation response, strength degradation and energy dissipation characteristics of CFS axial members. The new cyclic loading protocol was adapted from the FEMA 461 quasi-static cyclic loading protocol for structural components. The protocol anchor point is defined as the axial deformation that initiates buckling deformation in the seventh cycle, calculated with the global or cross-sectional slenderness before a test.

The amount of strength degradation, stiffness degradation, and pinching of the load–deformation response varies for the different specimens; however, the behavior is similar across the different buckling modes, lengths and cross-sections considered. The total energy dissipated within a damaged half-wave decreases with increasing cross-sectional slenderness. Strength degradation in compression occurred at similar rates for all the specimens, regardless of buckling mode. Unloading stiffness from compression was different for the different buckling modes and affected the amount of hysteretic pinching when reloading in tension.

and less cumulative axial deformation before fracture ($\Sigma\delta/L < 0.7$). In contrast, specimens with higher cross-sectional slenderness, e. g., 600LAC ($\lambda_{\ell} = 3.05$) and 600DAC ($\lambda_d = 1.53$), dissipate less energy within the damaged half-wave. Locally slender members (λ_{ℓ}, $\lambda_d > 1.3$) experience elastic buckling strains that leads to less damage accumulated per cycle and more cumulative axial deformation before fracture ($\Sigma\delta/L > 1.0$). Specimens experiencing global buckling (e.g., 600GAC and 362GAC) have the lowest energy dissipation capacity per half-wavelength and low cumulative axial
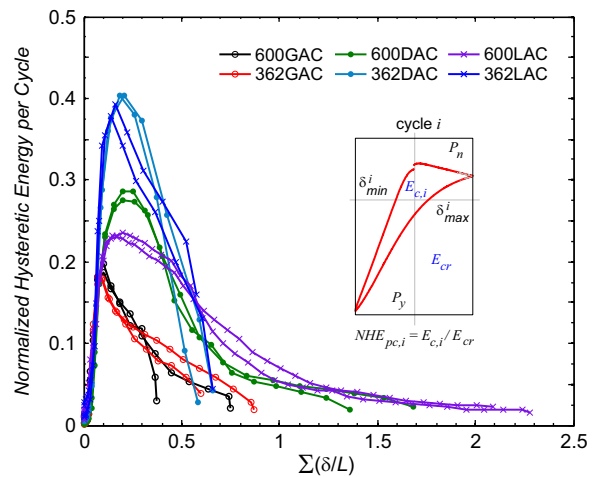
Table 6
Hysteretic energy dissipation.

Specimen	$HE_{0.25}$ (kN-mm)	$HE_{0.5}$	$HE_{1.0}$	HE_T	$HE_{0.25}/L_{cr}$ (kN-mm/mm)	$HE_{0.5}/L_{cr}$	$HE_{1.0}/L_{cr}$	HE_T/L_{cr}	max $\Sigma\delta/L$ ($\times 100$)
600S137-97-GAC-1	12,234	–	–	16,063	10.70	–	–	14.05	37
600S137-97-GAC-2	12,339	19,327	–	22,983	10.79	16.91	–	20.11	75
362S137-68-GAC-1	5676	10,176	–	14,952	4.97	8.90	–	13.08	87
362S137-68-GAC-2	5508	9078	–	10,009	4.82	7.94	–	8.76	60
600S137-68-DAC-1	3125	6191	8234	8935	12.06	23.90	31.78	34.49	136
600S137-68-DAC-2	2844	5800	7598	8960	11.00	22.43	29.38	34.65	168
362S137-68-DAC-1	3131	5846	–	6458	44.02	82.20	–	90.81	66
362S137-68-DAC-2	3614	6195	–	6368	50.81	87.11	–	89.55	58
600S162-33-LAC-1	630	1313	2033	2550	5.64	11.75	18.19	22.82	209
600S162-33-LAC-2	593	1248	1863	2344	5.33	11.22	16.74	21.07	228
362S162-54-LAC-1	1580	3270	–	3839	22.21	45.98	–	53.98	57
362S162-54-LAC-2	1767	3316	–	3773	24.67	46.29	–	52.68	66

HE_{xx}=cumulative hysteretic energy dissipated up to $\Sigma\delta/L=xx$.
HE_T=cumulative hysteretic energy dissipated until failure.
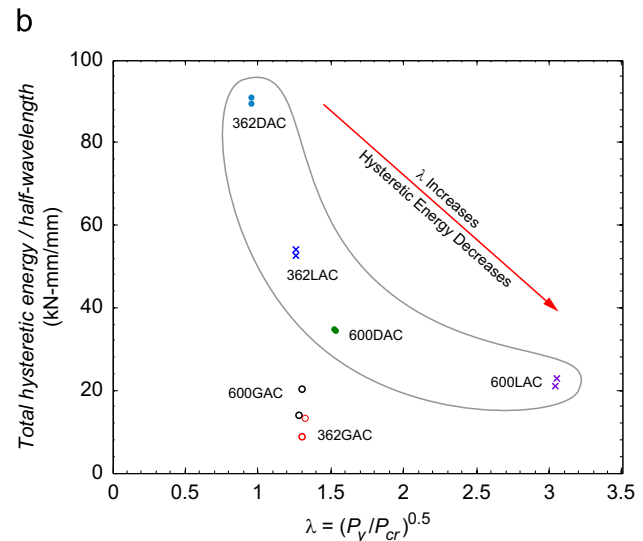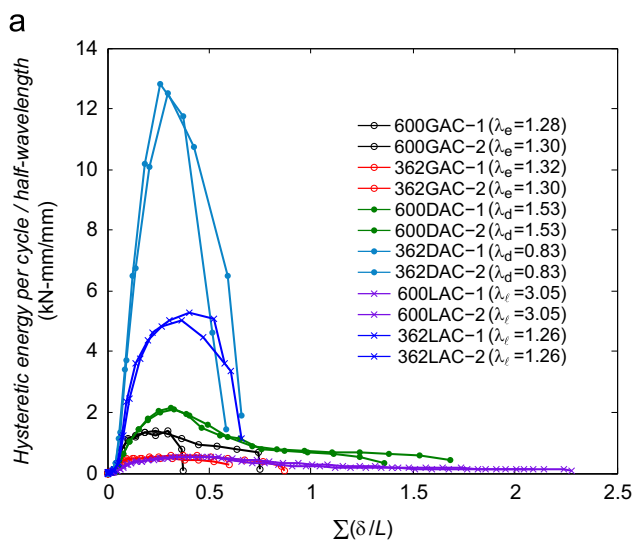

Fig. 15. Hysteretic energy per half-wavelength (HE_T/L_{cr}) vs. (a) cumulative axial deformation and (b) cross-sectional or global slenderness.

The experimental results summarized in this paper are being used by the authors to develop general load–deformation hysteretic numerical models capable of capturing the cyclic behavior of cold-formed steel axial members including strength and stiffness degradation.

References

[1] AISI S213-07. North American standard for cold-formed steel framing: lateral design. Washington, D.C.: American Iron and Steel Institute, ANSI/AISI-S213-07; 2007.
[2] Shamim I, Rogers CA. Numerical modeling and calibration of CFS framed shear walls under dynamic loading. In: Proceedings of the 21st international specialty conference on cold-formed steel structures. St. Louis, Missouri; October 24–25, 2012.
[3] Shamim I, Rogers CA. Steel sheathed/CFS framed shear walls under dynamic loading: numerical modelling and calibration. Thin-Walled Struct 2013;71 (0):57–71.
[4] Liu P, Peterman KD, Yu C, Schafer BW. Characterization of cold-formed steel shear wall behavior under cyclic loading for the CFS-NEES building. In: Proceedings of the 21st international specialty conference on cold-formed steel structures. St. Louis, Missouri; October 24–25, 2012.
[5] Madsen RL, Nakata N, Schafer BW. CFS-NEES building structural design narrative. Research report, RR01, access at ⟨www.ce.jhu.edu/cfsness⟩, October 2011, revised RR01c May 2012; 2011.
[6] FEMA, FEMA P695—quantification of building seismic performance factors. Document no. FEMA 965. Washington, D.C.: Federal Emergency Management Agency (FEMA);, 2009.
[7] FEMA, FEMA 461—interim protocols for determining seismic performance characteristics of structural and nonstructural components through laboratory testing. Document no. FEMA 461. Federal Emergency Management Agency (FEMA); 2007.
[8] Higginbotham AB, Hanson RD. Axial hysteretic behavior of steel members. J Struct Div 1976;102(7):1365–81.
[9] Ikeda K, Mahin SA. Cyclic response of steel braces. J Struct Eng 1986;112 (2):342.
[10] Tang X, Goel SC. Seismic analysis and design considerations of concentrically braced steel structures. Report no. UMCE 87-4. Ann Arbor, MI: Department of Civil Engineering, The University of Michigan; 1987.
[11] Papadrakakis M, Loukakis K. Elastic–plastic hysteretic behaviour of struts with imperfections. Eng Struct 1987;9(3):162–70.
[12] Nonaka T. An elastic–plastic analysis of a bar under repeated axial loading. Int J Solids Struct 1973;9(5):569–80.

[13] Sohal IS, Chen WF. Local buckling and inelastic cyclic behavior of tubular sections. Thin-Walled Struct 1988;6(1):63–80.

[14] Goel SC. Cyclic post-buckling behavior of steel bracing members. In: Fukumoto Y, Lee GC, editors. Stability and ductility of steel structures under cyclic loading, Boca Raton, FL: CRC Press; 1992. p. 75–84.

[15] Goggins JM, Broderick BM, Elghazouli AY, Lucas AS. Behaviour of tubular steel members under cyclic axial loading. J Constr Steel Res 2006;62(1–2):121–31.

[16] Popov EP, Black RG. Steel struts under severe cyclic loadings. J Struct Div 1981;107(9):1857–81.

[17] Jain AK, Hanson RD, Goel SC. Hysteretic cycles of axially loaded steel members. J Struct Div 1980;106(8):1777–95.

[18] Mahin Popov EP, Stephen A, Zayas VA. Cyclic inelastic buckling of thin tubular columns. J Struct Div 1979;105(11):2261–77.

[19] Yao T, Nikolov PI. Numerical experiment on buckling/plastic collapse behavior of plates under cyclic loading. In: Fukumoto Y, Lee GC, editors. Stability and ductility of steel structures under cyclic loading, Boca Raton, FL: CRC Press; 1992. p. 203–14.

[20] Usami T, Ge HB. Cyclic behavior of thin-walled steel structures—numerical analysis. Thin-Walled Struct 1998;32(1–3):41–80.

[21] Watanabe E, Sugiura K, Mori T, ``Suzuki I. Modeling of hysteretic behavior of thin-walled box members.'' In: Fukumoto Y, Lee GC, editors. Stability and ductility of steel structures under cyclic loading. Boca Raton, FL: CRC Press; 1992; p. 225–35.

[22] Calderoni B, De Martino A, Formisano A, Fiorino L. Cold formed steel beams under monotonic and cyclic loading: experimental investigation. J Constr Steel Res 2009;65(1):219–27.

[23] AISI-S100-07. North American specification for the design of cold-formed steel structural members. Washington, D.C.: American Iron and Steel Institute. ANSI/AISI-S100-07; 2007.

[24] SSMA Steel Stud Manufacturers Association. Product technical information. ICBO ER-4943P. ⟨http://www.ssma.com⟩ 15.12.11.

[25] Moen CD. Direct strength design for cold-formed steel members with perforations [Ph.D. dissertation]. Baltimore: Johns Hopkins University; 2008.

[26] Schafer BW, Adany S. Buckling analysis of cold-formed steel members using CUFSM: conventional and constrained finite strip methods. In: Proceedings of the 18th international specialty conference on cold-formed steel structures. Orlando, FL, United states: University of Missouri-Rolla; 2006.

[27] ASTM E8M-04. Standard test methods for tension testing of metallic materials (Metric). West Conshohocken, PA: ASTM International; 2004.

[28] Moncarz PD, Krawinkler H. Theory and application of experimental model analysis in earthquake engineering. The John A. Blume Earthquake Engineering Center Report No. 50; 1981.

[29] AISI-S910-08. Test method for distortional buckling of cold-formed steel hat shaped compression members. Washington, D.C.: American Iron and Steel Institute. ANSI/AISI-S910-08; 2008.

[30] Moen CD, Schafer BW. Experiments on cold-formed steel columns with holes. Thin-Walled Struct 2008;46(10):1164–82.

[31] Zeinoddini VM. Geometric imperfections in cold-formed steel members [Ph.D. dissertation]. Baltimore: Johns Hopkins University; 2011.

[32] Padilla-Llano DA, Moen CD, Eatherton MR. Energy dissipation of thin-walled cold-formed steel members. Research Report No. CE/VPI-ST-13/06. Blacksburg, VA: Virginia Polytechnic Institute and State University; 2013.

[33] ASTM-C955. Standard specification for load-bearing (transverse and axial) steel studs, runners (tracks), and bracing or bridging for screw application of gypsum panel products and metal plaster bases. West Conshohocken, PA; 2009.

[34] Moen CD, Igusa T, Schafer BW. Prediction of residual stresses and strains in cold-formed steel members. Thin-Walled Struct 2008;46(11):1274–89.

[35] Schafer BW, Pekoz T. Computational modeling of cold-formed steel: characterizing geometric imperfections and residual stresses. J Constr Steel Res 1998;47(3):193–210.

[36] VTechWorks. ⟨http://hdl.handle.net/10919/18721⟩; May 2012.